LETTERS

Seismic evidence for widespread western-US deep-crustal deformation caused by extension

M. P. Moschetti[1]†, M. H. Ritzwoller[1], F. Lin[1] & Y. Yang[1]

Laboratory experiments have established that many of the materials comprising the Earth are strongly anisotropic in terms of seismic-wave speeds[1]. Observations of azimuthal[2,3] and radial[4,5] anisotropy in the upper mantle are attributed to the lattice-preferred orientation of olivine caused by the shear strains associated with deformation, and provide some of the most direct evidence for deformation and flow within the Earth's interior. Although observations of crustal radial anisotropy would improve our understanding of crustal deformation and flow patterns resulting from tectonic processes, large-scale observations have been limited to regions of particularly thick crust[6]. Here we show that observations from ambient noise tomography in the western United States reveal strong deep (middle to lower)-crustal radial anisotropy that is confined mainly to the geological provinces that have undergone significant extension during the Cenozoic Era (since ~65 Myr ago)[7,8]. The coincidence of crustal radial anisotropy with the extensional provinces of the western United States suggests that the radial anisotropy results from the lattice-preferred orientation of anisotropic crustal minerals caused by extensional deformation. These observations also provide support for the hypothesis that the deep crust within these regions has undergone widespread and relatively uniform strain in response to crustal thinning and extension[9–11].

To infer information about crustal anisotropy in the western United States from surface-wave dispersion requires measurements at periods less than 20 s, but waves at these periods are strongly scattered and attenuated as they propagate from distant earthquakes. Because surface waves with periods greater than 20 s are primarily sensitive to wave-speed structures below a depth of ~25 km, only regions with very thick crust have been amenable to the inversion of surface-wave data for crustal radial anisotropy[6]. The inference of the three-dimensional distribution of anisotropy in regions with normal to thin continental crust is now possible, however, using surface-wave dispersion measurements at periods from 6 to 20 s recovered from ambient seismic noise[12,13]. The dispersion data from ambient noise tomography have been combined with longer period (>40-s) Rayleigh-wave phase-speed measurements from multiple-plane-wave earthquake tomography to generate high-resolution images of isotropic S-wave speeds in the crust and uppermost mantle across the western United States[14]. We show similarly high-resolution images of the radial anisotropy of the crust and uppermost mantle in the western United States and discuss implications for deformation within the deep crust.

We follow the ambient noise data-processing protocol of ref. 15 to obtain cross-correlations between long time series (of lengths up to several years) of ambient noise recorded at pairs of seismic stations of the USArray Transportable Array. The cross-correlations provide three-component, interstation 'empirical Green's functions' from which measurements of Rayleigh- and Love-wave group and phase speeds are obtained at periods from 6 to 40 s (refs 16, 17). These measurements are strongly sensitive to S-wave speeds in the crust and uppermost mantle and facilitate the imaging of structures shallower than those typically resolved using teleseismic earthquake observations alone[18]. At each point in time, the Transportable Array comprises about 400 broadband stations on a 70 km × 70 km grid (Fig. 1a). We processed waveforms from 526 Transportable Array stations acquired between October 2004 and December 2007 to obtain Rayleigh- and Love-wave dispersion measurements along more than 120,000 interstation paths (Supplementary Fig. 1). Love-wave group-speed measurements are less reliable than the others, and we retain only measurements of the other speeds in certain period bands, as follows: Rayleigh-wave group and phase speeds, 6–40 s; Love-wave phase speeds, 8–32 s. Inversion of the dispersion measurements begins with the construction of dispersion maps. The maps based on dispersion measurements from ambient noise (see, for example, Figs 1b–d) are constructed using a traditional straight-ray tomographic method[19]. Measurement of Rayleigh-wave phase speeds by multiple-plane-wave earthquake tomography is described in ref. 14, but the maps have been updated to extend the study area and to incorporate data from additional earthquakes. The combined period band of the Rayleigh-wave phase-speed measurements extends from 6 to 100 s.

We report results of inversions for radial anisotropy (transverse isotropy with a radial symmetry axis) in the crust and uppermost mantle underlying the western United States. Radial anisotropy, also referred to as polarization anisotropy, manifests itself as the difference in the speeds of horizontally and vertically polarized, horizontally propagating S waves (V_{SH} and V_{SV}, respectively). It is inferred by simultaneously interpreting the dispersion characteristics of Rayleigh and Love waves, which depend predominantly on V_{SV} and V_{SH}, respectively. In particular, it is inferred from the 'Rayleigh–Love discrepancy', which is a measure of the mis-fit to the Rayleigh- and Love-wave dispersion curves that results from a best-fitting isotropic model (in which $V_{SH} = V_{SV} = V_S$, the S-wave speed).

To illustrate the existence and nature of the Rayleigh–Love discrepancy in the western United States and to localize its source, we present three inversions. Inversion I defines a purely isotropic reference state in which there is a single S-wave speed at each depth in the crust and upper mantle. Inversion II is a perturbation of the isotropic reference model in which radial anisotropy is permitted in the upper mantle but not in the crust. Inversion III further perturbs the model by allowing radial anisotropy in the crust with an additional perturbation in the upper mantle. In each case, the data are the same: local dispersion curves, with uncertainties (Methods), that are constructed from the dispersion maps on a 0.5° × 0.5° grid across the study region (see, for example, Fig. 2a for a point in central Nevada). Forward modelling is performed using the radially anisotropic code

[1]Center for Imaging the Earth's Interior, Department of Physics, University of Colorado at Boulder, Campus Box 390, Boulder, Colorado 80309, USA. †Present address: Geologic Hazards Science Center, US Geological Survey, Denver, Colorado 80225, USA.

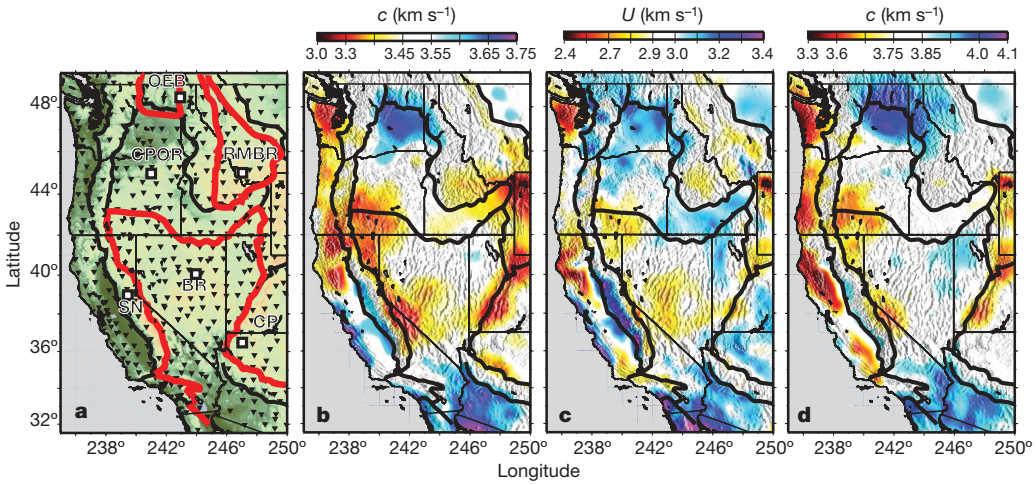

Figure 1 | Major tectonic regions and example surface-wave dispersion in the study region. **a**, Western US study region. Seismic stations (black triangles), major tectonic boundaries (thick black lines) and boundaries of the predominant extensional provinces (Basin and Range (BR), Rocky Mountain basin and range (RMBR) and Omineca extended belt (OEB); red lines) are identified. Grid points from the BR, the Columbia Plateau in Oregon (CPOR), the Colorado Plateau (CP), the OEB, the RMBR and the Sierra Nevada (SN) are indicated by white squares. Examples from Figs 2 and 4 correspond to these grid points. **b**–**d**, Maps of Rayleigh-wave phase speed (**b**), Rayleigh-wave group speed (**c**) and Love-wave phase speed (**d**) at a period of 20 s. *c*, phase speed; *U*, group speed.

MINEOS[20] and the model space is sampled by a Monte Carlo method[21].

An example best-fitting model for a point in central Nevada produced using inversion I is shown in Fig. 2b. Because data at periods greater than 30 s are generally well fitted by the isotropic models of inversions I, II and III, we present the reduced chi-squared mis-fit, χ^2, in the 6–30-s period band. The range of acceptable models for this point, and how those models fit the dispersion data, is shown in Supplementary Fig. 3a, b. The isotropic models from inversion I produce a large Rayleigh–Love discrepancy across most of the western United States, as seen in Fig. 2c. The spatially averaged chi-squared mis-fit from the best-fitting model of inversion I is $\chi^2_{\rm I} = 12.2$. At locations with large chi-squared values (for example the point in central Nevada in Fig. 2a, for which $\chi^2 = 29.2$), Love-wave phase speeds computed from the isotropic model underestimate the observed speeds at periods greater than ~15 s, whereas the Rayleigh-wave phase and group speeds are slightly overestimated at periods between 20 and 30 s and severely overestimated at periods less than 20 s. Because more measurements of Rayleigh waves than Love waves are inverted, the isotropic model tends to fit the Rayleigh-wave data better than the Love-wave data.

Inversion II attempts to resolve this Rayleigh–Love discrepancy by introducing radial anisotropy in the upper mantle as a single depth-independent perturbation between $V_{\rm SH}$ and $V_{\rm SV}$. We permit radial anisotropy with an amplitude ($2|V_{\rm SH} - V_{\rm SV}|/(V_{\rm SH} + V_{\rm SV})$) of up to 10%, consistent with the largest values observed in ref. 22. The introduction of mantle anisotropy (see, for example, Fig. 2e) improves the data fit significantly ($\chi^2 = 10.5$; Fig. 2d, f) in comparison with the isotropic model, reducing the overall mis-fit to $\chi^2_{\rm II} = 5.7$, which is a 77% variance reduction. Regions of relatively poor data fit persist, however. Residual mis-fit to the Rayleigh-wave phase and group speeds is largest at periods less than ~15 and ~20 s, respectively, whereas mis-fit to the Love-wave phase speeds remains largest at periods between ~15 and ~25 s (see, for example, Fig. 2d). The

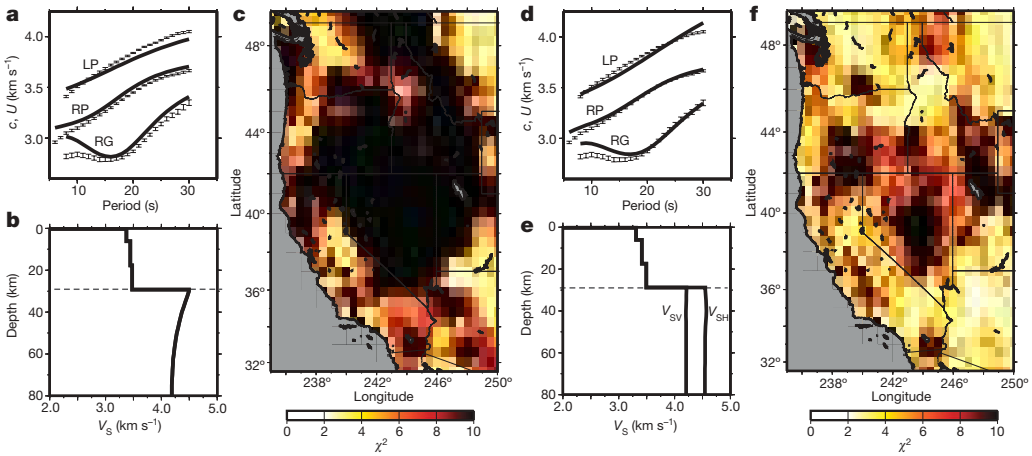

Figure 2 | Mis-fit to surface-wave dispersion data from inversions I and II, which do not include crustal radial anisotropy. **a**, **b**, Example local dispersion curves (with 1σ error bars, **a**) compared with black curves predicted by the best-fitting isotropic model, Inversion I, from the BR (**b**). LP, Love-wave phase speed; RG, Rayleigh-wave group speed; RP, Rayleigh-wave phase speed. The mis-fit in **a** reflects the Rayleigh–Love discrepancy and identifies the need for radial anisotropy. **c**, Chi-squared mis-fit for the best-fitting model from Inversion I; spatially averaged mis-fit, $\chi^2_{\rm I} = 12.2$. **d**, Same as **a**, but fitted curves are from inversion II, which includes radial anisotropy in the mantle. **e**, Same as **b**, but from inversion II. **f**, Same as **c**, but from Inversion II; spatially averaged mis-fit, $\chi^2_{\rm II} = 5.7$. The Rayleigh–Love discrepancy is partially resolved by introducing mantle radial anisotropy.

amplitude of radial anisotropy in the mantle that results from this inversion is shown in Supplementary Fig. 4.

Significant further reduction in the Rayleigh–Love discrepancy requires the introduction of radial anisotropy in the crust. The inability of other physically reasonable model parameters to resolve the discrepancy is demonstrated in Supplementary Information. In inversion III, we perturb the best-fitting model from inversion II by allowing a constant anisotropic perturbation of middle- and lower-crustal S-wave speeds and an additional perturbation of mantle anisotropy. With this inversion, there is a trade-off between the amplitudes of radial anisotropy in the crust and mantle; the resulting amplitudes of crustal and mantle anisotropy are negatively correlated across all tectonic regions, as indicated by the negative slopes of the mis-fit ellipses shown in Fig. 3. In some regions (for example the Sierra Nevada and much of the Colorado Plateau; Fig. 3b, c) radial anisotropy is not required in either the crust or the mantle to fit the data, whereas in other regions (for example the region of the Columbia Plateau lying in Oregon; Fig. 3a) it is. However, in extensional provinces in the western United States (for example the Basin and Range province, the Rocky Mountain basin and range, and the Omineca extended belt), positive crustal anisotropy ($V_{SH} > V_{SV}$; Fig. 3d–f) is required irrespective of the strength of the mantle anisotropy. Although the amplitude of the crustal anisotropy in these regions depends on the amplitude of the mantle anisotropy, the sign of the crustal radial anisotropy is unique and positive. We refer to the regions with unambiguously positive crustal radial anisotropy as the 'anisotropic crustal regions'. Outside the anisotropic crustal regions, crustal anisotropy is generally not required by the data.

To construct a single model using inversion III, we constrain upper-mantle anisotropy to lie within 2% of the best-fitting model from inversion II (Supplementary Fig. 4). Because of the negative correlation between crustal and mantle anisotropy, this constraint produces a conservative (lower-bound) estimate of the amplitude of crustal anisotropy. Example results for central Nevada are shown in Fig. 4a, b ($\chi^2 = 3.2$). The mean amplitudes of radial anisotropy in the crust and mantle across the anisotropic crustal regions are 3.6% and 5.3%, respectively. Only positive radial anisotropy is observed. Mis-fit resulting from inversion III is presented in Fig. 4c, and the mean chi-squared mis-fit across the study region is $\chi^2_{III} = 2.8$, which is a 95% variance reduction relative to the isotropic model from inversion I. The introduction of crustal radial anisotropy resolves the residual Rayleigh–Love discrepancy to $\chi^2 < 4$, on average, except in discrete areas outside the primary anisotropic crustal regions where other structural variables may need to be introduced to improve the data fit further (for example the Olympic peninsula, the Great Valley of California, the Salton Trough, parts of the High Lava Plains of Oregon, the southern Cascades and Yellowstone National Park). Residual mis-fit is discussed further in ref. 23.

The amplitudes of crustal and mantle radial anisotropy in the best-fitting model from inversion III are shown in Fig. 4d, e. The resulting patterns of strong crustal radial anisotropy correlate with the predominant extensional provinces in the region. Cenozoic extension in the western United States is believed to have been primarily confined to the Basin and Range province, the Rocky Mountains basin and range, and the Omineca extended belt[7] (Fig. 1a). Average extension across these provinces has been estimated to range up to 100% (refs 7, 8). Strong crustal radial anisotropy is evident across nearly the entire Basin and Range province and terminates abruptly near its edges, for example along the Wasatch and Sierra Nevada ranges, along the Snake River plain and along the Colorado Plateau. Crustal anisotropic amplitudes greater than 5% are present in all three extensional provinces. The largest continuous region of high-amplitude radial crustal anisotropy (>4%) occurs in central Nevada. Observations of seismic anisotropy in the mantle are routinely ascribed to the lattice-preferred orientation of mantle minerals and are used to infer characteristics about the mantle flow field[24,25]. Because of the relative dearth of observations of middle- to lower-crustal anisotropy, such inferences are not common for the crust.

Various studies, however, suggest widespread lower-crustal deformation in response to extension in the western United States[9–11]. Heretofore, regional-scale observations of crustal seismic anisotropy have not existed to support or overturn this hypothesis. We interpret the observed crustal radial anisotropy as resulting from the lattice-preferred orientation of seismically anisotropic crustal minerals induced by the finite strains accompanying extension. The shear strains associated with crustal extension preferentially orient the seismic slow axes along the vertical axis[26]. At middle to lower crustal depths, microfractures are closed by lithostatic stresses[27] and the lattice-preferred

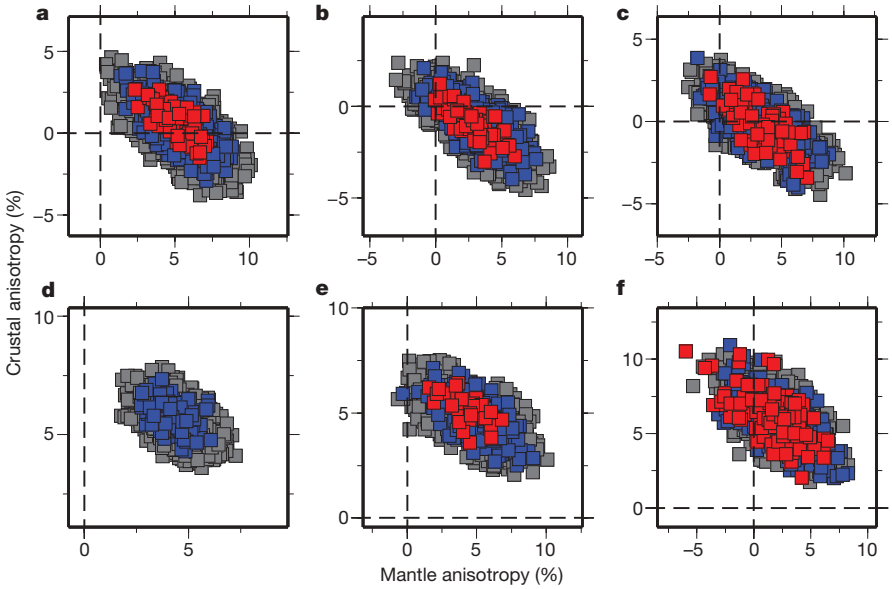

Figure 3 | Crustal radial anisotropy within the extensional provinces is required despite a trade-off between the amplitudes of crustal and mantle radial anisotropy. Mis-fit ellipses reflecting trade-off between amplitudes of crustal and mantle radial anisotropy resulting from inversions with no constraints on the amplitudes of anisotropy in the crust or mantle. Symbol colours correspond to chi-squared mis-fit: grey, $3.0 \leq \chi^2 < 4.0$; blue, $2.0 \leq \chi^2 < 3.0$; red, $\chi^2 < 2.0$. **a**, CPOR; **b**, SN; **c**, CP; **d**, BR; **e**, RMBR; **f**, OEB. The locations BR, RMBR and OEB lie within the principal extensional provinces of the western United States.

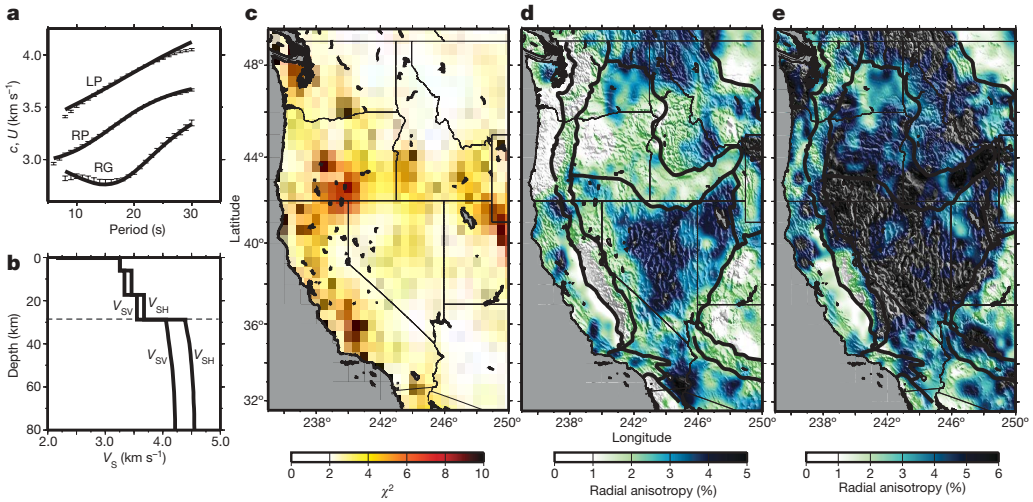

Figure 4 | Data mis-fit and the amplitude of radial anisotropy in the crust and upper mantle using inversion III. Here crustal and mantle radial anisotropy are allowed. **a**, Same as Fig. 2a, d, but for inversion III. **b**, Same as Fig. 2b, e, but for inversion III. **c**, Same as Fig. 2c, f, but for the best-fitting model from inversion III; spatially averaged mis-fit, $\chi^2_{III} = 2.8$. The observed Rayleigh–Love discrepancy is largely resolved by introducing crustal radial anisotropy in addition to mantle anisotropy. **d**, **e**, Amplitudes of radial anisotropy ($2|V_{SH} - V_{SV}|/(V_{SH} + V_{SV})$) from inversion III for the crust (**d**) and for the mantle (**e**). Tectonic province boundaries are indicated with black lines.

orientations of micas and amphiboles significantly contribute to seismic anisotropy[1,26,28]. Improved vertical resolution of radial anisotropy is needed to estimate the contributions from specific minerals in this region. Our results suggest, however, that the deep-crustal response to extension in the western United States is widespread and relatively uniform.

METHODS SUMMARY

For a radially anisotropic medium, the elasticity tensor reduces to a symmetric matrix with twelve non-zero elements and five independent components. These five components may be represented by the Love parameters, A, C, F, L and N (ref. 29). Horizontally propagating seismic-wave speeds are given by $V_{PH} = (A/\rho)^{1/2}$, $V_{SH} = (N/\rho)^{1/2}$ and $V_{SV} = (L/\rho)^{1/2}$, where ρ is density. The dimensionless parameters $\xi = N/L = (V_{SH}/V_{SV})^2$, $\phi = C/A = (V_{PV}/V_{PH})^2$ and $\eta = F/(A - 2L)$ are commonly introduced and in an isotropic medium all equal one (V_{PH} and V_{PV} are the speeds of horizontally and vertically propagating P waves, respectively). Because surface-wave dispersion measurements are less sensitive to ϕ and η than to ξ, we perturb only ξ from its isotropic value. We find that perturbations of the ϕ and η parameters do not significantly affect our conclusions (Supplementary Information).

Rayleigh- and Love-wave dispersion curves are simultaneously inverted using the radially anisotropic code MINEOS[20] to calculate surface-wave dispersion curves and the neighbourhood algorithm[21] for model-space sampling. We invert for layer thicknesses, for V_P/V_S, for V_{SH} and V_{SV} in the crust, and for V_{SH} and V_{SV} in the mantle. Uniform model parameterizations and constraints are applied at all grid points. Models are parameterized using four crustal layers (one sedimentary and three underlying crystalline layers) and five cubic B-splines in the mantle. We impose a layer thickness ratio of 1:2:2 for the crystalline crustal layers. Independent perturbations of the thicknesses of the sediment and crystalline layers are allowed, but total crustal thickness is constrained by receiver function estimates and uncertainties[30]. Crustal S-wave speeds increase monotonically with depth. The values of V_P/V_S, V_{SH} and V_{SV} are constrained within physically reasonable bounds summarized in Supplementary Table 1.

Full Methods and any associated references are available in the online version of the paper at www.nature.com/nature.

Received 31 October 2009; accepted 17 February 2010.

1. Siegesmund, S., Takeshita, T. & Kern, H. Anisotropy of V_P and V_S in an amphibolite of the deeper crust and its relationship to the mineralogical, microstructural and textural characteristics of the rock. *Tectonophysics* **157,** 25–38 (1989).
2. Montagner, J.-P. & Tanimoto, T. Global upper mantle tomography of seismic velocities and anisotropies. *J. Geophys. Res.* **96,** 20,337–20,351 (1991).
3. Silver, P. G. Seismic anisotropy beneath the continents: probing the depths of geology. *Annu. Rev. Earth Planet. Sci.* **24,** 385–421 (1996).
4. Ekström, G. & Dziewonski, A. M. The unique anisotropy of the Pacific upper mantle. *Nature* **394,** 168–172 (1998).
5. Shapiro, N. M. & Ritzwoller, M. H. Monte-Carlo inversion for a global shear-velocity model of the crust and upper mantle. *Geophys. J. Int.* **151,** 88–105 (2002).
6. Shapiro, N. M., Ritzwoller, M. H., Molnar, P. H. & Levin, V. Thinning and flow of Tibetan crust constrained by seismic anisotropy. *Science* **305,** 233–236 (2004).
7. Wernicke, B. in *The Cordilleran Orogen: Conterminous US* (eds Burchfiel, B. C., Lipman, P. W. & Zoback, M. L.) 553–581 (Geol. Soc. Am., 1992).
8. Janecke, S. U. Translation and breakup of supradetachment basins: lessons from Grasshopper, Horse Prairie, Medicine Lodge, Muddy Creek and Nicholia Creek Basins, SW Montana. *Geol. Soc. Am. Abstr. Prog.* **36,** 546 (2004).
9. Block, L. & Royden, L. H. Core complex geometries and regional scale flow in the lower crust. *Tectonics* **9,** 557–567 (1990).
10. Bird, P. Lateral extrusion of the lower crust from under high topography, in the isostatic limit. *J. Geophys. Res.* **96,** 10,275–10,286 (1991).
11. Kruse, S., McNutt, M., Phipps-Morgan, J., Royden, L. & Wernicke, B. Lithospheric extension near Lake Mead, Nevada: a model for ductile flow in the lower crust. *J. Geophys. Res.* **96,** 4435–4456 (1991).
12. Sabra, K. G., Gerstoft, P., Roux, P., Kuperman, W. A. & Fehler, M. C. Surface wave tomography from microseisms in Southern California. *Geophys. Res. Lett.* **32,** L14311 (2005).
13. Shapiro, N. M., Campillo, M., Stehly, L. & Ritzwoller, M. H. High-resolution surface-wave tomography from ambient seismic noise. *Science* **307,** 1615–1618 (2005).
14. Yang, Y., Ritzwoller, M. H., Lin, F.-C., Moschetti, M. P. & Shapiro, N. M. The structure of the crust and uppermost mantle beneath the western US revealed by ambient noise and earthquake tomography. *J. Geophys. Res.* **113,** B12310 (2008).
15. Bensen, G. D. *et al.* Processing seismic ambient noise data to obtain reliable broad-band surface wave dispersion measurements. *Geophys. J. Int.* **169,** 1239–1260 (2007).
16. Moschetti, M. P., Ritzwoller, M. H. & Shapiro, N. M. Surface wave tomography of the western United States from ambient seismic noise: Rayleigh wave group velocity maps. *Geochem. Geophys. Geosyst.* **8,** Q08010 (2007).
17. Lin, F., Moschetti, M. P. & Ritzwoller, M. H. Surface wave tomography of the western United States from ambient seismic noise: Rayleigh and Love wave phase velocity maps. *Geophys. J. Int.* **173,** 281–298 (2008).
18. Yang, Y. & Ritzwoller, M. H. Teleseismic surface wave tomography in the western US using the Transportable Array component of USArray. *Geophys. Res. Lett.* **5,** L04308 (2008).
19. Barmin, M. P., Ritzwoller, M. H. & Levshin, A. L. A fast and reliable method for surface wave tomography. *Pure Appl. Geophys.* **158,** 1351–1375 (2001).
20. Masters, G., Barmine, M. P. & Kientz, S. *Mineos: User Manual* (Calif. Inst. Technol., 2007).
21. Sambridge, M. Geophysical inversion with a neighbourhood algorithm – I. Searching a parameter space. *Geophys. J. Int.* **138,** 479–494 (1999).
22. Nettles, M. & Dziewonski, A. M. Radially anisotropic shear velocity structure of the upper mantle globally and beneath North America. *J. Geophys. Res.* **113,** B02303 (2008).
23. Moschetti, M. P., Ritzwoller, M. H., Lin, F. & Yang, Y. Crustal shear velocity structure of the western US inferred from ambient seismic noise and earthquake data. *J. Geophys. Res.* (submitted).
24. Silver, P. G. & Holt, W. E. The mantle flow field beneath western North America. *Science* **295,** 1054–1057 (2002).

25. Becker, T. W., Schulte-Pelkum, V., Blackman, D. K., Kelloff, J. B. & O'Connell, R. J. Mantle flow under the western United States from shear wave splitting. *Earth Planet. Sci. Lett.* **247,** 235–251 (2006).
26. Mainprice, D. & Nicolas, A. Development of shape and lattice preferred orientations: application to the seismic anisotropy of the lower crust. *J. Struct. Geol.* **11,** 175–189 (1989).
27. Rasolofosaon, P. N. J., Rabbel, W., Siegesmund, S. & Vollbrecht, A. Characterization of crack distribution: fabric analysis versus ultrasonic inversion. *Geophys. J. Int.* **141,** 413–424 (2000).
28. Weiss, T., Siegesmund, S., Rabbel, W., Bohlen, T. & Pohl, M. Seismic velocities and anisotropy of the lower continental crust: a review. *Pure Appl. Geophys.* **156,** 97–122 (1999).
29. Love, A. E. H. *A Treatise on the Theory of Elasticity* 4th edn, 298–300 (Cambridge Univ. Press, 1927).
30. Gilbert, H. J. & Fouch, M. J. Complex upper mantle seismic structure across the southern Colorado Plateau/Basin and Range II: results from receiver function analysis. *Eos* **88** (Fall meeting), abstr. S41B–0558 (2007).

Supplementary Information is linked to the online version of the paper at www.nature.com/nature.

Acknowledgements This manuscript benefited from discussions with K. Mahan, C. Jones and P. Molnar. Research was supported by the US National Science Foundation, Division of Earth Sciences. M.P.M. received support from an US National Defense Science and Engineering Graduate Fellowship from the American Society for Engineering Education. The facilities of the IRIS Data Management System, and specifically the IRIS Data Management Center, were used to access the waveform and metadata required in this study.

Author Contributions M.P.M. carried out ambient noise tomography for the Rayleigh-wave measurements, performed the three-dimensional inversion of surface-wave dispersion measurements and co-wrote the paper. M.H.R. guided the study design and co-wrote the paper. F.L. carried out ambient noise tomography for the Love-wave measurements. Y.Y. carried out the multiple-plane-wave earthquake tomography. All authors discussed the results and provided comments on the manuscript.

Author Information Reprints and permissions information is available at www.nature.com/reprints. The authors declare no competing financial interests. Correspondence and requests for materials should be addressed to M.P.M. (mmoschetti@usgs.gov).

METHODS

Inversion of surface-wave dispersion measurements for a three-dimensional S-wave speed model proceeds in two steps: (1) the inversion of surface-wave dispersion measurements from the interstation empirical Green's functions by ambient noise tomography (ANT) and from earthquake data by multiple-plane-wave earthquake tomography (MPWT), to produce dispersion maps; and (2) inversion of the dispersion maps for the three-dimensional S-wave speed model. Inversions I, II and III differ only in the amplitudes of radial anisotropy allowed in the deep (middle to lower) crust and in the uppermost mantle.

Surface-wave dispersion maps. Although we make use of two methods to construct surface-wave dispersion maps (ANT and MPWT), both techniques yield similar things—maps of surface-wave phase and group speeds as a function of period and geographic location. To calculate the dispersion maps by ANT, we have increased the number of stations and, therefore, the areal coverage relative to previously published results[16,17]. In addition, time series durations are increased by up to one year. All cross-correlations between 526 stations from the Transportable Array are calculated for the time period between October 2004 and December 2007 by established methods[15]. Dispersion measurements on the more than 120,000 empirical Green's functions are made by automated frequency–time analysis[15,31] and inverted using straight-ray tomography[19]. The resulting Rayleigh- and Love-wave maps span the period bands 6–40 s and 8–32 s, respectively.

MPWT is an extension of the two-plane-wave tomography method[32] to larger geographic regions. The Rayleigh-wave phase-speed maps from MPWT have been updated from published maps[14] to provide dispersion measurements across the western United States. To construct the Rayleigh-wave phase-speed maps (25–100-s period) using MPWT, 250 earthquakes were recorded at the Transportable Array between January 2006 and September 2008. At periods between 25 s and 40 s, for which Rayleigh-wave phase speeds are estimated by both ANT and MPWT, Yang *et al.*[14] demonstrate substantial agreement between the phase-speed estimates and equivalent resolution in the dispersion maps.

Data uncertainty estimates. To assess data mis-fit and select the set of accepted models, uncertainty estimates are required for group- and phase-speed maps as a function of position, period and wave type. Uncertainty estimation for ANT is discussed in detail in ref. 23. Supplementary Fig. 2a–d shows example uncertainty maps for Rayleigh-wave phase speed at periods of 8, 16, 24 and 40 s. Uncertainties for Rayleigh-wave phase speeds from MPWT are derived from inversion residuals following ref. 14 and show little spatial variability; the spatial average uncertainty is plotted in Supplementary Fig. 2e. As described in ref. 23 for ANT, Rayleigh-wave group-speed and Love-wave phase-speed uncertainties are estimated by a frequency-dependent scaling of the Rayleigh-wave phase-speed uncertainty maps of ref. 33. The scaling parameters derive from the temporal variability of each measurement type as discussed in ref. 15. Uncertainty maps for Rayleigh-wave group speed and Love-wave phase speed, therefore, have the same spatial pattern as shown for Rayleigh-wave phase speeds in Supplementary Fig. 2a–d. Spatially averaged uncertainties for all three speeds are presented, as functions of period, in Supplementary Fig. 2f. The spatially averaged and frequency-averaged uncertainties in the Rayleigh-wave phase-speed, Rayleigh-wave group speed and Love-wave phase-speed maps from ANT are 14.5, 38.1 and 13.4 m s^{-1}, respectively. The spatially averaged and frequency-averaged uncertainty in the Rayleigh-wave phase-speed maps from MPWT is 27.6 km s^{-1}.

Inversions for S-wave speed. The Rayleigh-wave phase- and group-speed maps and the Love-wave phase-speed maps are inverted simultaneously on a $0.5^\circ \times 0.5^\circ$ grid across the study region to a depth of 250 km, where the model ties into the S-wave speed model of ref. 5. Inversion parameters include V_P/V_S, V_{SH}, V_{SV} and crustal layer thicknesses, in the crust, and V_{SH} and V_{SV}, in the mantle. Because we find that upper-crustal anisotropy cannot resolve the Rayleigh–Love discrepancy, we require the sedimentary and uppermost crystalline crustal layer to be isotropic. Allowed ranges for the inversion parameters are presented in Supplementary Table 1. Crustal thicknesses are constrained by the range provided by receiver function estimates and uncertainties[30]. Details of the inversion are provided in ref. 23. The inversion uses the neighbourhood algorithm[21] for parameter-space sampling and the radially anisotropic MINEOS[20] code for calculation of surface-wave dispersion curves. At least 500,000 trial models, subject to the constraints of Supplementary Table 1, are forward-modelled at each grid point. Selection of the final set of models is determined by data mis-fit, as described below. Inversions I, II and III differ in the amplitudes of radial anisotropy allowed in the deep (middle to lower) crust and in the uppermost mantle. Inversion I is an isotropic model, inversion II allows radial anisotropy in the uppermost mantle and inversion III allows radial anisotropy in the deep crust and uppermost mantle.

Model acceptance criteria. At each spatial grid point, and for each of the three inversions, we accept a set of models that fit the dispersion curves within a specified mis-fit threshold. We define this threshold to be two units greater than the reduced chi-squared mis-fit, $\chi^2 = n^{-1} \sum_{i=1}^{n} \sigma_i^{-2}(d_i - p_i)^2$, of the best-fitting model. Here, n is the number of discrete dispersion measurements along the dispersion curves, d_i are the observed local dispersion values, p_i are the predicted dispersion values from a trial model and σ_i are the measurement errors. At each grid point, we require a minimum of 1,000 models to be accepted for the final set of models.

31. Levshin, A. L., Pisarenko, V. F. & Pogrebinsky, G. A. On a frequency-time analysis of oscillations. *Ann. Geophys.* **28,** 211–218 (1972).
32. Forsyth, D. & Li, A. in *Seismic Earth: Array Analysis of Broadband Seismograms* (eds Levander, A. & Nolet, G.) 81–97 (Geophys. Monogr. 157, Am. Geophys. Union, 2005).
33. Lin, F., Ritzwoller, M. H. & Snieder, R. Eikonal tomography: surface wave tomography by phase front tracking across a regional broad-band seismic array. *Geophys. J. Int.* **177,** 1091–1110 (2009).